Electronic Supplementary Material (ESI) for Energy & Environmental Science.

Supplementary Information

Twisted Grain Boundary Leads to High Thermoelectric Performance in Tellurium Crystal

Stanley Abbey[1,10], Hanhwi Jang[2,10], Brakowaa Frimpong[1], Naveen Kumar[3], Woo Hyun Nam[4], Van Quang Nguyen[5], Jong Ho Park[6], Chien Viet Nguyen[7], Hosun Shin[7], Jae Yong Song[7], Su-Dong Park[6], Sunglae Cho[5], Chandan Bera[3], Jaimin Kang[2], Byong-Guk Park[2], Muath Al Malki[8,9], G. Jeffrey Snyder[8], Yeon Sik Jung[2], Ki-Ha Hong[1], and Min-Wook Oh[1*]

[1] Department of Materials Science and Engineering, Hanbat National University, 125 Dongseodae-ro, Yuseong-gu, Daejeon 34158, Republic of Korea ㅓ|

[2] Department of Materials Science and Engineering, Korea Advanced Institute of Science and Technology (KAIST), Daejeon 34141, Republic of Korea

[3] Institute of Nano Science & Technology, Knowledge City, Sector-81, SAS Nagar, Mohali 140306, Punjab, India

[4]Energy Efficiency Materials Center, Korea Institute of Ceramic Engineering and Technology (KICET), Jinju 52851, Republic of Korea

[5] Department of Physics and Energy Harvest-Storage Research Center, University of Ulsan, Ulsan, 44610, Republic of Korea

[6]Thermoelectric Conversion Center, Creative and Fundamental Research Division, Korea Electrotechnology Research Institute (KERI), Changwon 51543, Republic of Korea

[7] Korea Research Institute of Standards and Science (KRISS), Daejeon 34113, Republic of Korea

[8] Department of Materials Science and Engineering, Northwestern University, Illinois 60208, USA

[9] King Fahd University of Petroleum and Minerals, Dhahran 31261, Saudi Arabia

[10] These authors contributed equally: Stanley Abbey, Hanhwi Jang

*Corresponding author e-mail: mwoh@hanbat.ac.kr

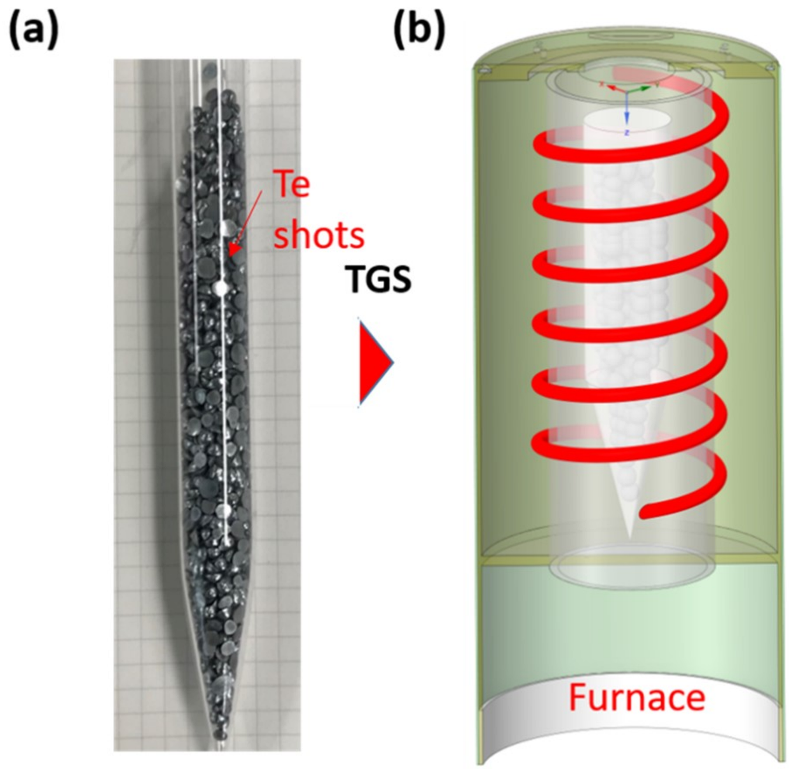

Supplementary Fig. 1| Schematic representation of the synthesis of ingots. (a) Sealed sample of Te and Fe_2As powder as received. (b) Diagram of temperature gradient solidification furnace designed in house.

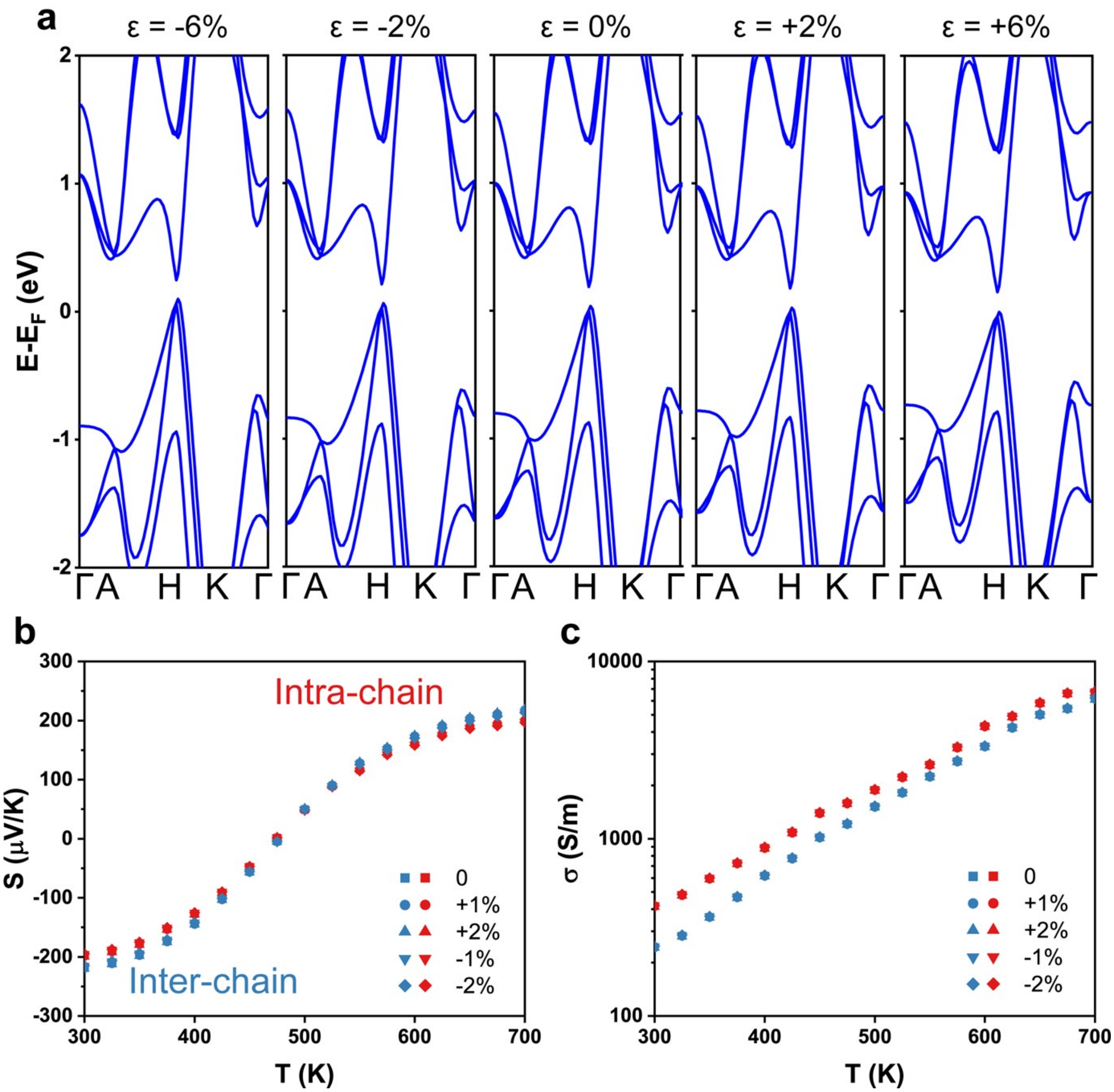

Supplementary Fig. 2| Strain-dependent electronic properties of Te. (a) Calculated electronic band structure of Te without spin-orbit interaction under uniaxial strain along the c-axis ranging from -6 to 6%. Note that the strain effect on the band edge position is dominant at Γ and A points, while marginal at H point. (b-c) Calculated temperature-dependent (b) Seebeck coefficient and (c) electrical conductivity for various magnitude of uniaxial strain.

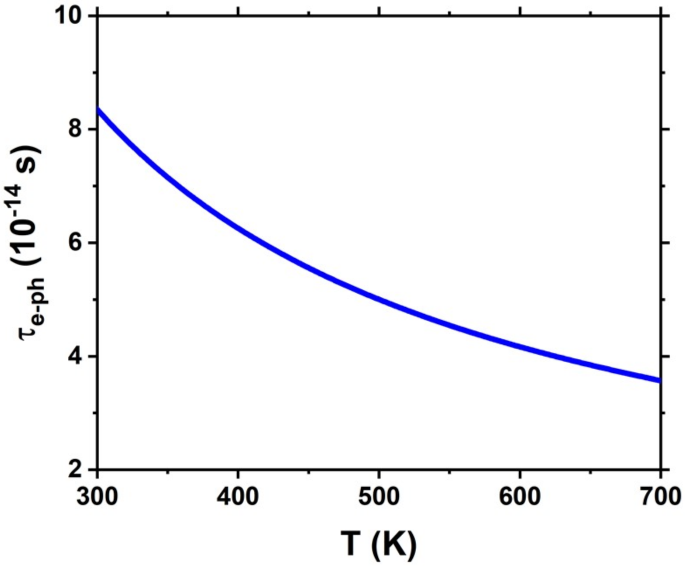

Supplementary Fig. 3| Variation of relaxation time of tellurium as a function of temperature for electron-phonon scattering

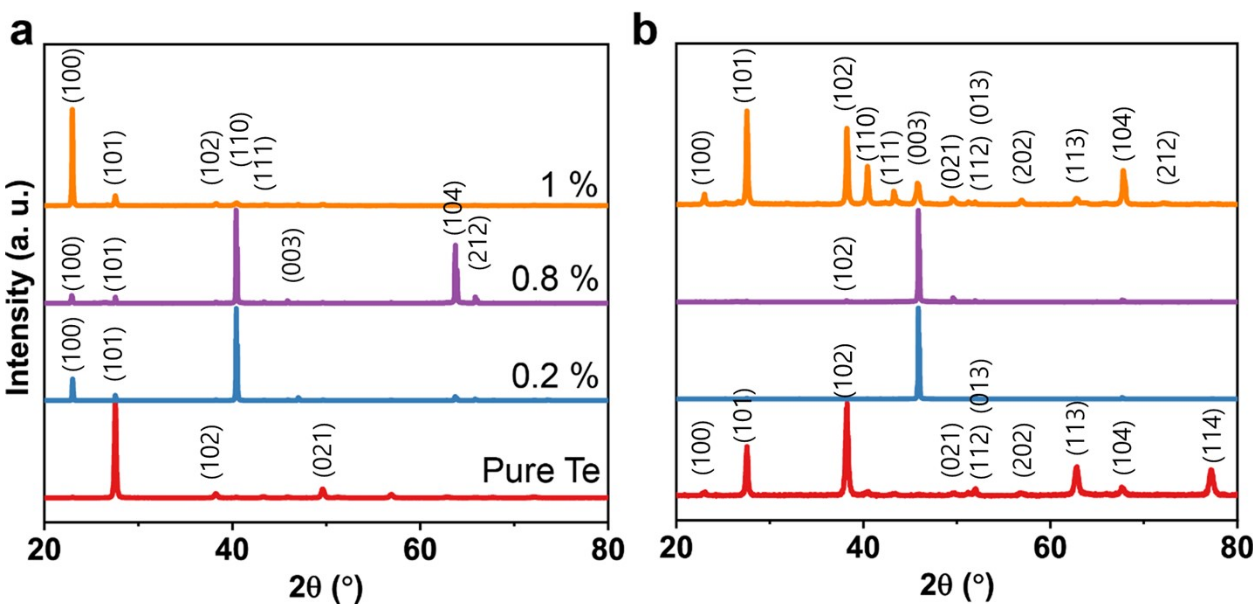

Supplementary Fig. 4| XRD patterns of Te crystals for various dopant concentrations measured along (a) parallel and (b) perpendicular to the growth direction, respectively

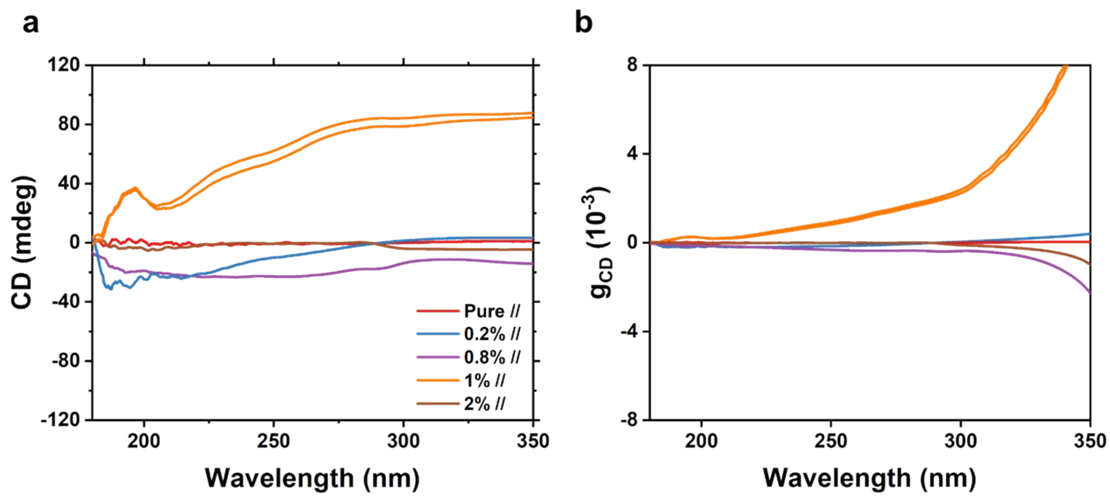

Supplementary Fig. 5| (a) Circular dichroism and (b) corresponding asymmetry factor (g_{CD}) spectra of pure and Fe_2As-doped Te. An absence of optical activity in the pure sample signifies that the optical activity measured in 1% Fe_2As-doped Te is not resulting from a chiral crystal structure of Te. The spectra for 1% Fe_2As-doped Te were measured for two different samples to confirm the reproducibility of the measurement.

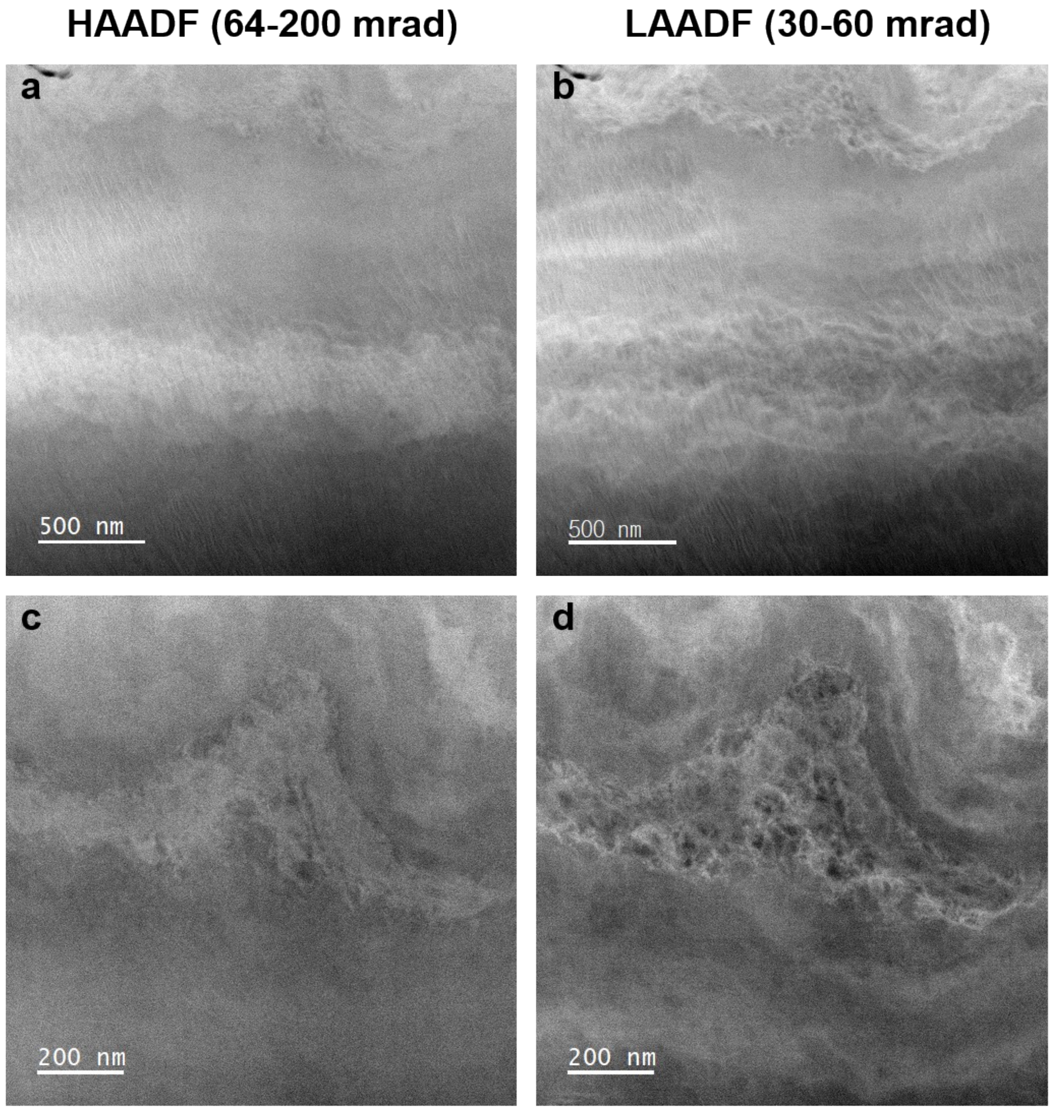

Supplementary Fig. 6| Contrast difference between (a, c) HAADF and (b, d) LAADF-STEM image of the 1% Fe_2As-doped Te without processing. Because the prepared TEM sample thickness is approximately 40 nm, strain contrast is positive in LAADF and negative in HAADF imaging. Note that streaks in (c) and (d) are attributed to milling artifacts made by Ga ion during the focused ion beam (FIB) process.

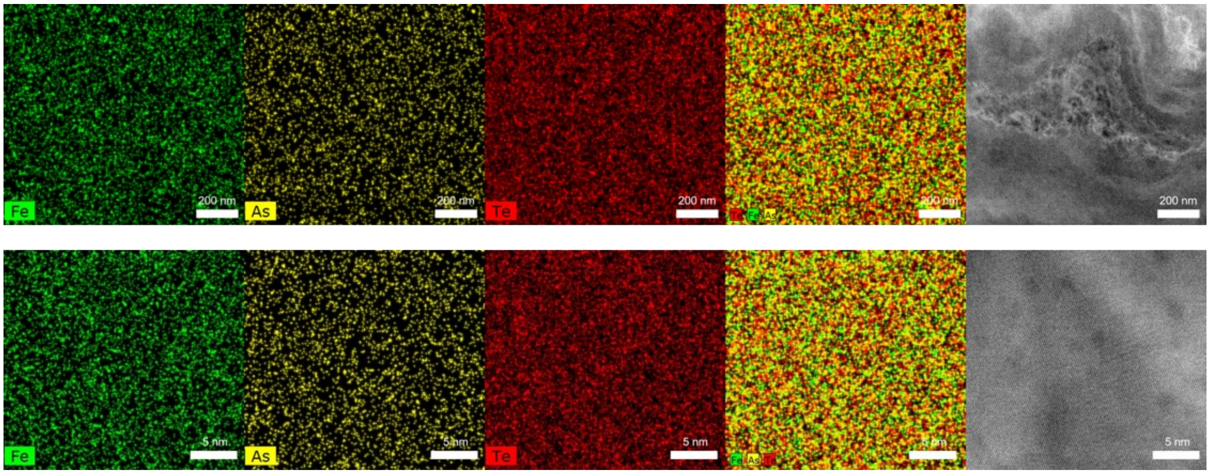

Supplementary Fig. 7| EDX elemental mapping of Fe (green), As (yellow), Te (red), mixed, and HAADF–STEM image of 1% Fe_2As-doped Te at a different magnification. No segregation or secondary phase detected in the specimen.

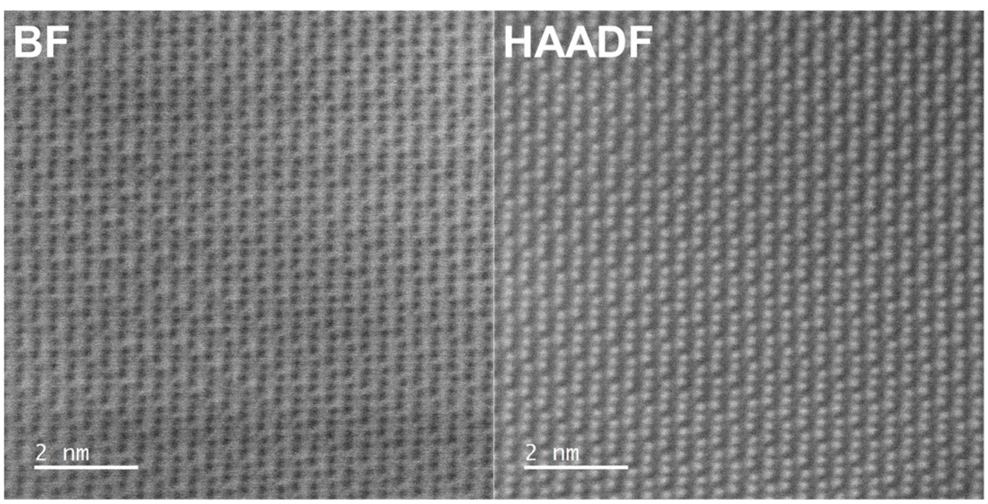

Supplementary Fig. 8| Unprocessed BF- and HAADF-STEM images of pure Te viewed along the [010] zone axis. Note that we used identical sample preparation protocols and equipment, and the sample was examined immediately after the Fe_2As-doped sample using the same apparatus (Titan cubed G2 80-300). The collection semi-angle was not changed for comparison.

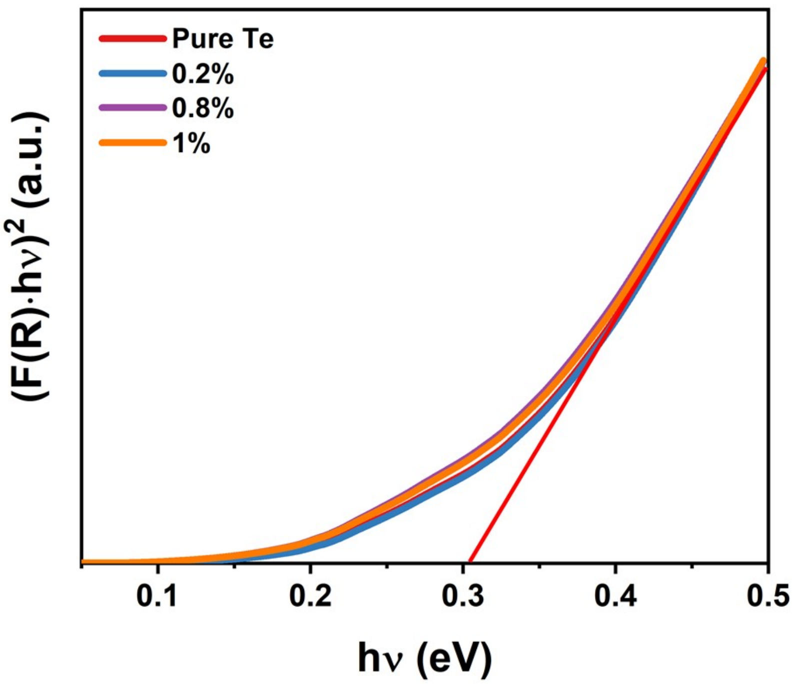

Supplementary Fig. 9| Diffuse reflectance infrared spectra of pure and Fe_2As-doped Te, showing an unchanged optical band gap of ~0.3 eV upon doping.

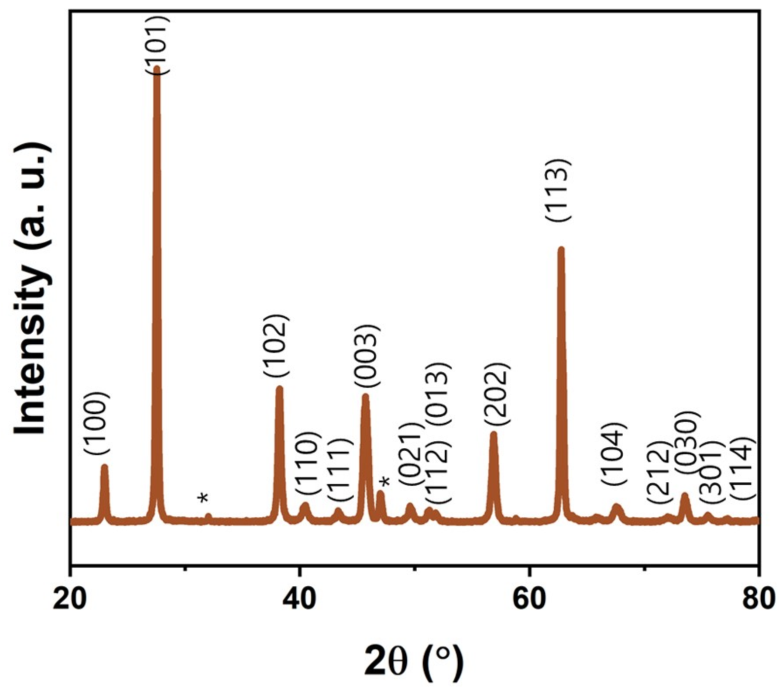

Supplementary Fig. 10| XRD patterns of 2% Fe_2As-doped Te crystal measured along the parallel to the growth direction. Adding excess amount of dopant decreases the degree of texturing and make the overall thermoelectric properties similar to the those of polycrystalline Te. Asterisk (*) symbol denotes the peak emerging from the As_2Te_3 secondary phase.

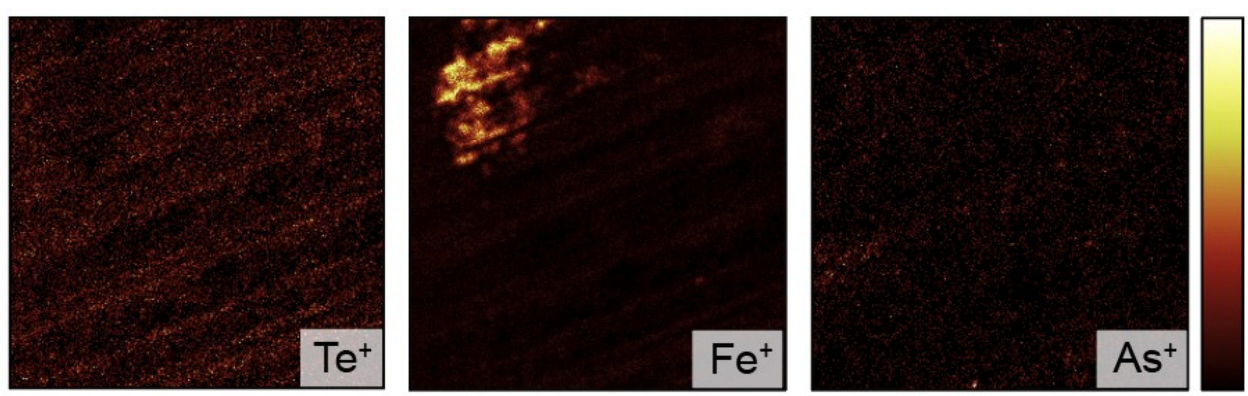

Supplementary Fig. 11| Time-of-flight–secondary ion mass spectroscopy (TOF-SIMS) elemental mapping of Te^+, Fe^+, and As^+ ions for an area equal to 100 × 100 μm^2. Fe-rich precipitates were observed, but As-related precipitates were not found in this analysis.

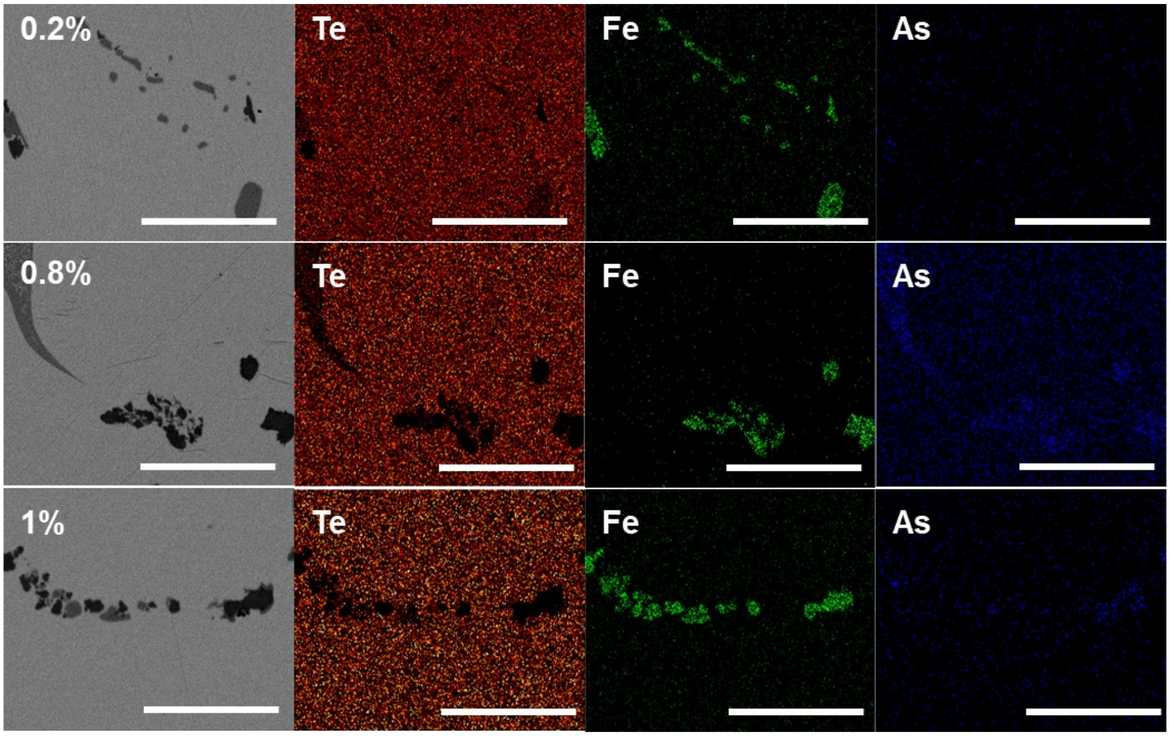

Supplementary Fig. 12| Back-scattered electron (BSE) image of polished surface for x = 0.2%, 0.8% and 1% Fe_2As with corresponding EDX elemental mapping showing the random distribution of Fe and As elements in Te matrix (scale bar = 60 μm). We observed inhomogeneous distribution of secondary phases in the Te matrix.

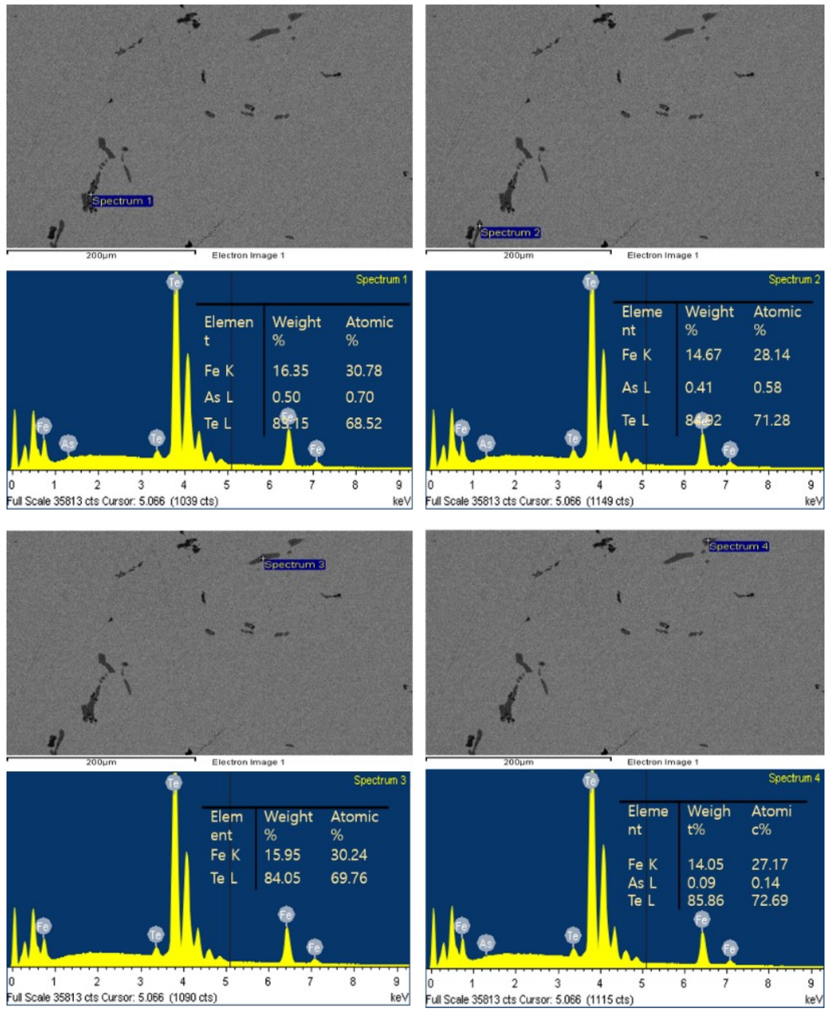

Supplementary Fig. 13| BSE-SEM of a polished surface of 1% Fe_2As showing phases of $FeTe_2$ inclusions. The respective EDX point analysis indicated in spectra 1 to 4 shows $FeTe_2$ precipitates in the matrix of Te owing to the limited solubility of Fe and As in the Te matrix.

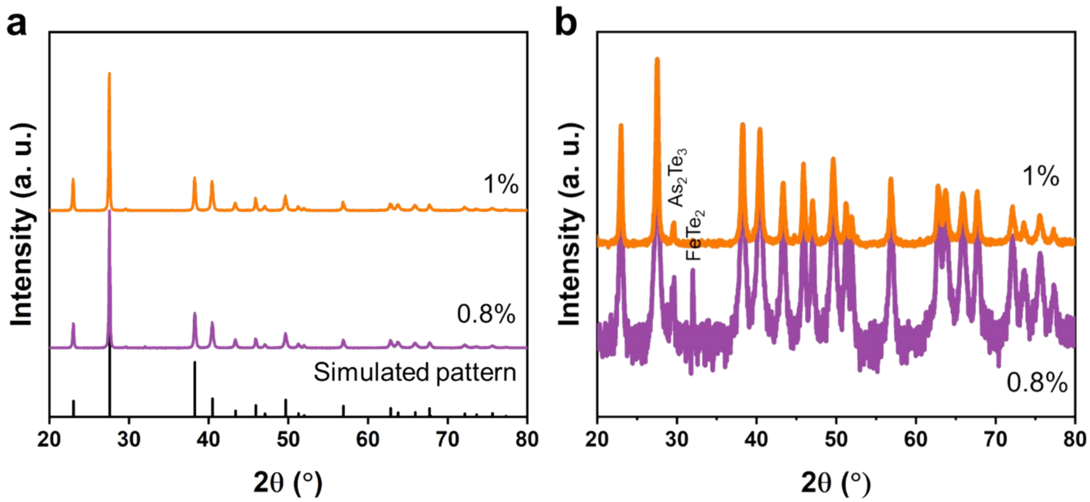

Supplementary Fig. 14| (a) Powder XRD profile for 0.8 % and 1% Fe_2As indicating the presence of secondary phases of As_2Te_3 and $FeTe_2$ peaks. The secondary phases indicate limited solubility of Fe and As in the Te matrix (<1 at. %). Note that the intensity in (b) is identical spectra with (a) but plotted on a log scale for visibility of peaks emerging from secondary phases.

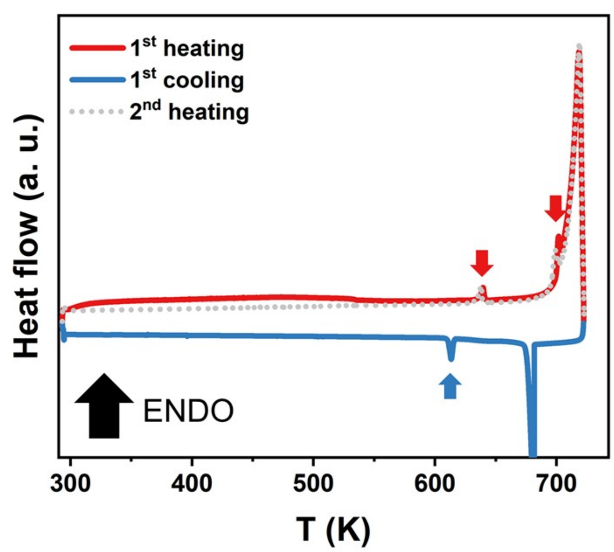

Supplementary Fig. 15| Differential scanning calorimetry (DSC) analysis on 1% Fe_2As doped Te. The red arrows denote endothermic heat flow from the crystallization of As_2Te_3 and reaction in the Fe-As phase.

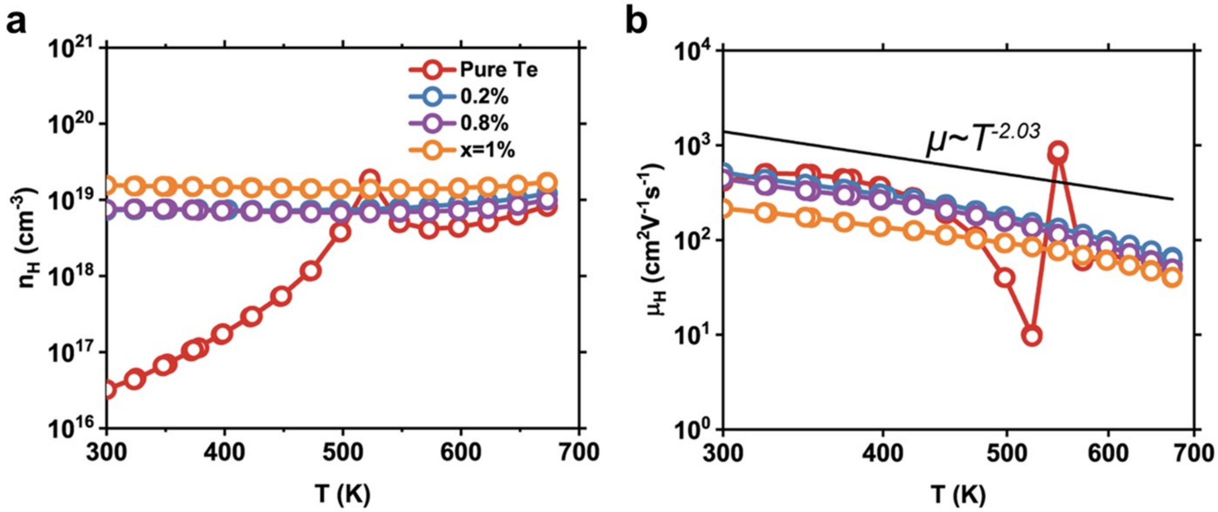

Supplementary Fig. 16| Temperature-dependent (a) Hall carrier concentration and (b) Hall mobility of pure and Fe_2As-doped Te. The $T^{-2.03}$ dependence of Hall mobility implies that the electron-phonon scattering is the dominant mechanism associated with the conduction process.

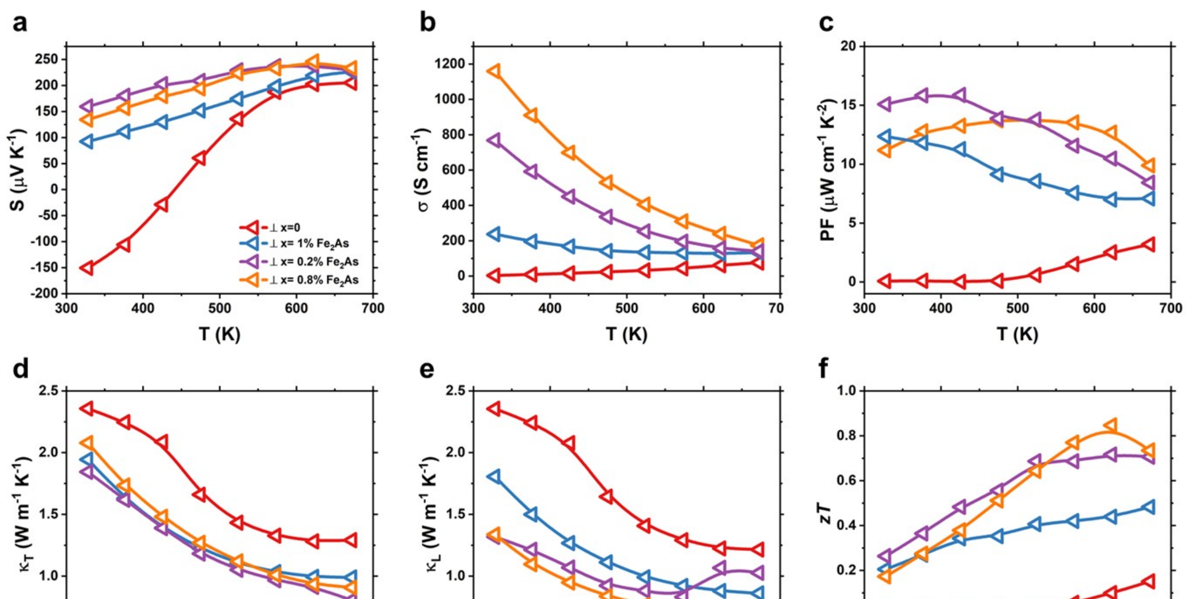

Supplementary Fig. 17| Temperature-dependent (a) Seebeck coefficient, (b) electrical conductivity, (c) total thermal conductivity, and (d) lattice thermal conductivity of pure and Fe_2As-doped Te along the direction perpendicular to the growth direction.

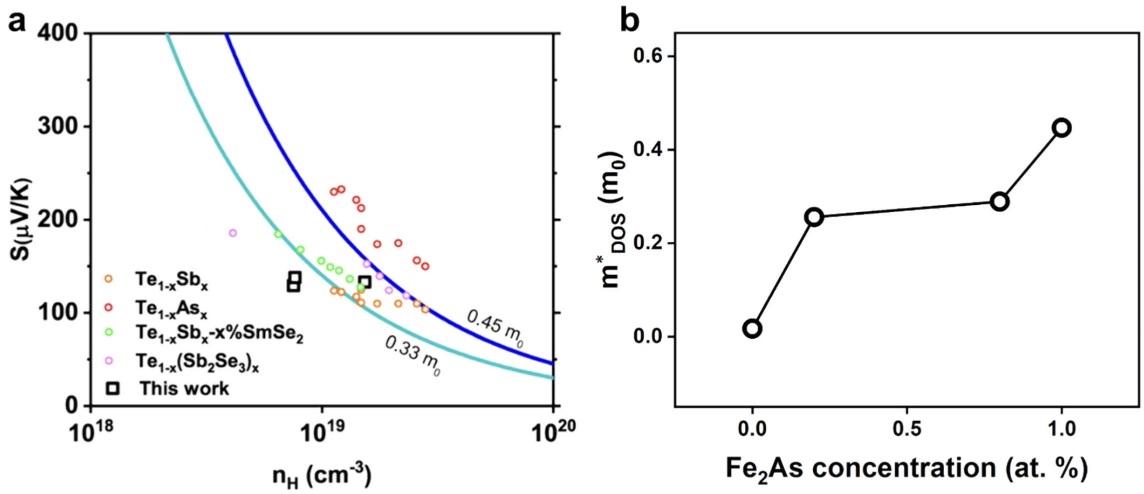

Supplementary Fig. 18| (a) Relationship of Seebeck coefficient and Hall carrier concentration (Pisarenko plot). and (b) the estimated density-of-states effective mass. The increase of the effective mass is attributed to the stronger nested band effect in a deeper Fermi level.

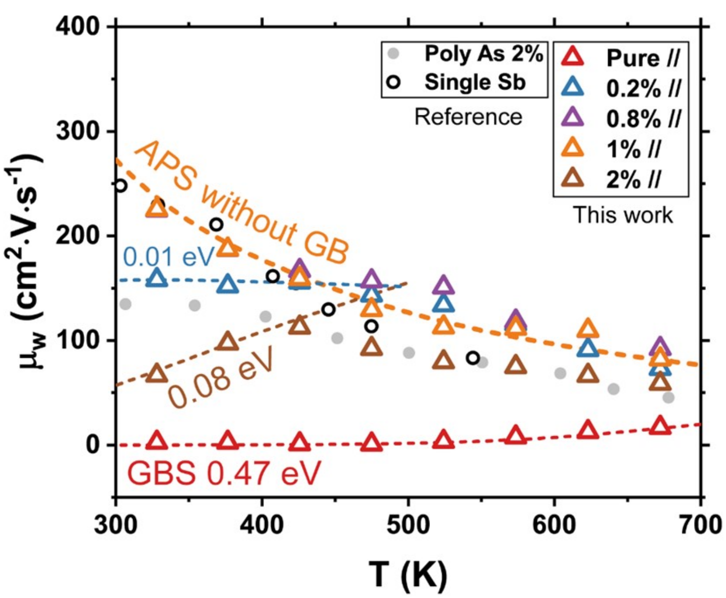

Supplementary Fig. 19| Temperature-dependent weighted mobility of pure and Fe_2As-doped Te. Dotted lines are fitted weighted mobility values for acoustic phonon scattering and grain boundary scattering at a given barrier height. The data for single-crystal and polycrystalline Te doped with Sb and As are plotted together for comparison.

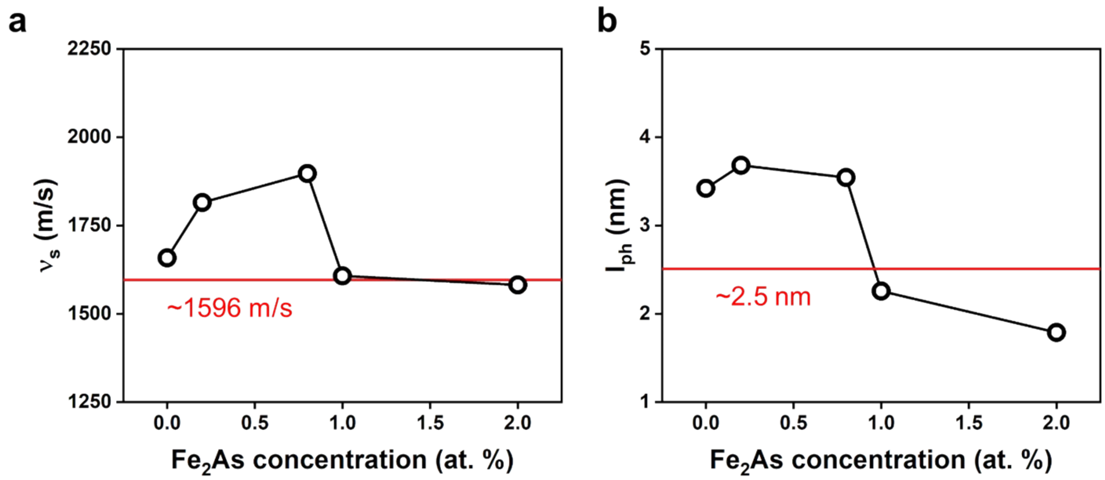

Supplementary Fig. 20| (a) The measured sound velocity and (b) the calculated phonon mean free path for pure and Fe_2As-doped Te samples along the parallel direction. The red solid line denotes a value reported polycrystalline Te.

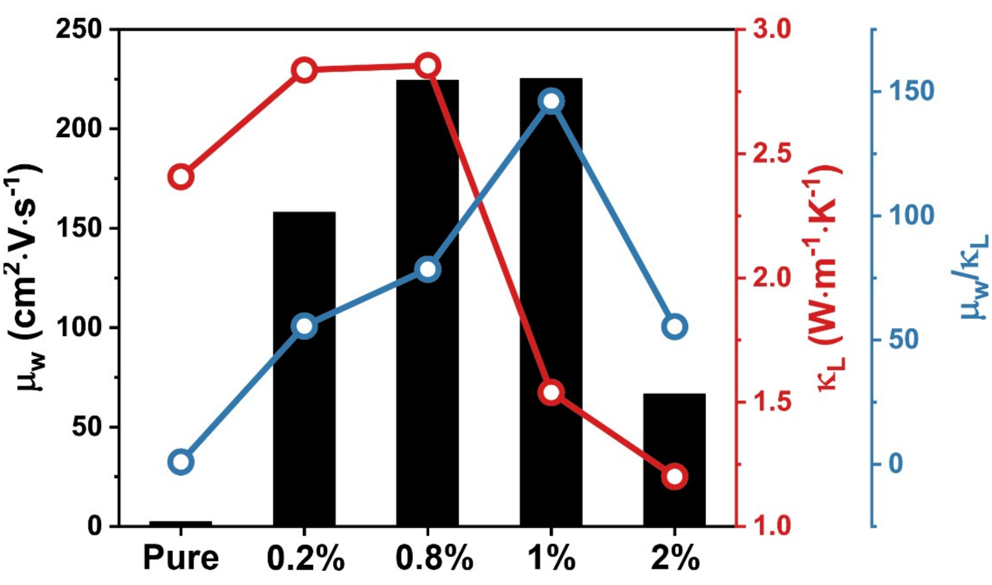

Supplementary Fig. 21| Weighted mobility, lattice thermal conductivity, and its ratio at 323 K for pure and Fe_2As-doped Te.

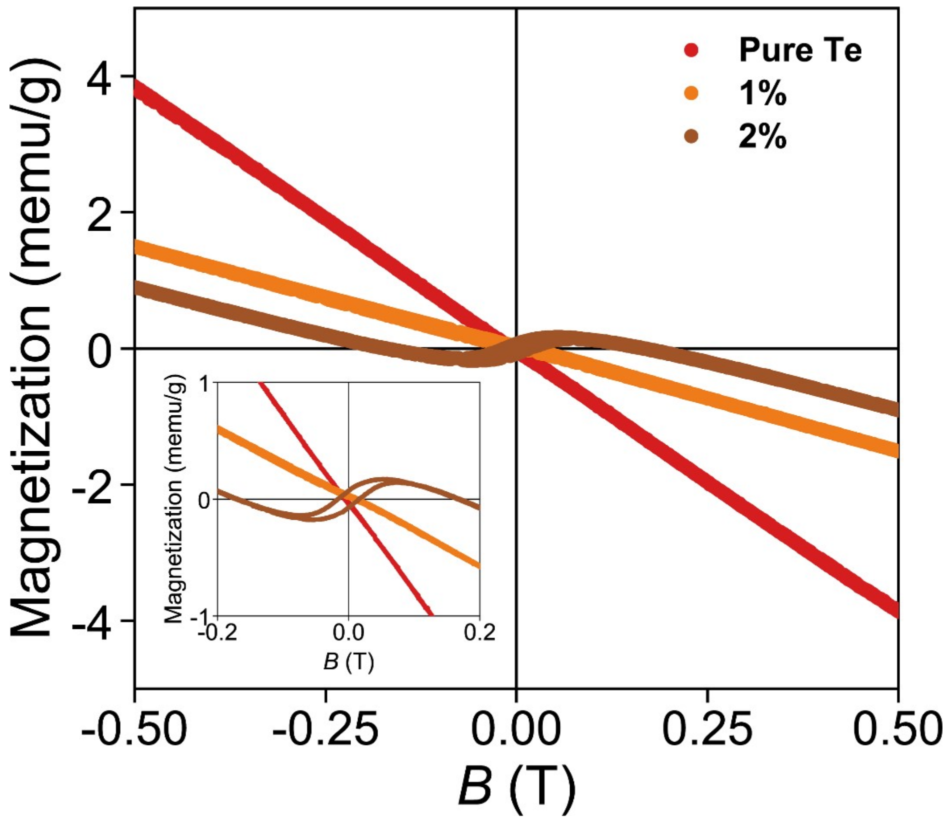

Supplementary Fig. 22| Hysteresis loop measurements of pure Te, 1%, and 2% Fe_2As-doped Te powder samples at 300 K. The inset shows an expanded view of the magnetization as a function of magnetic field.

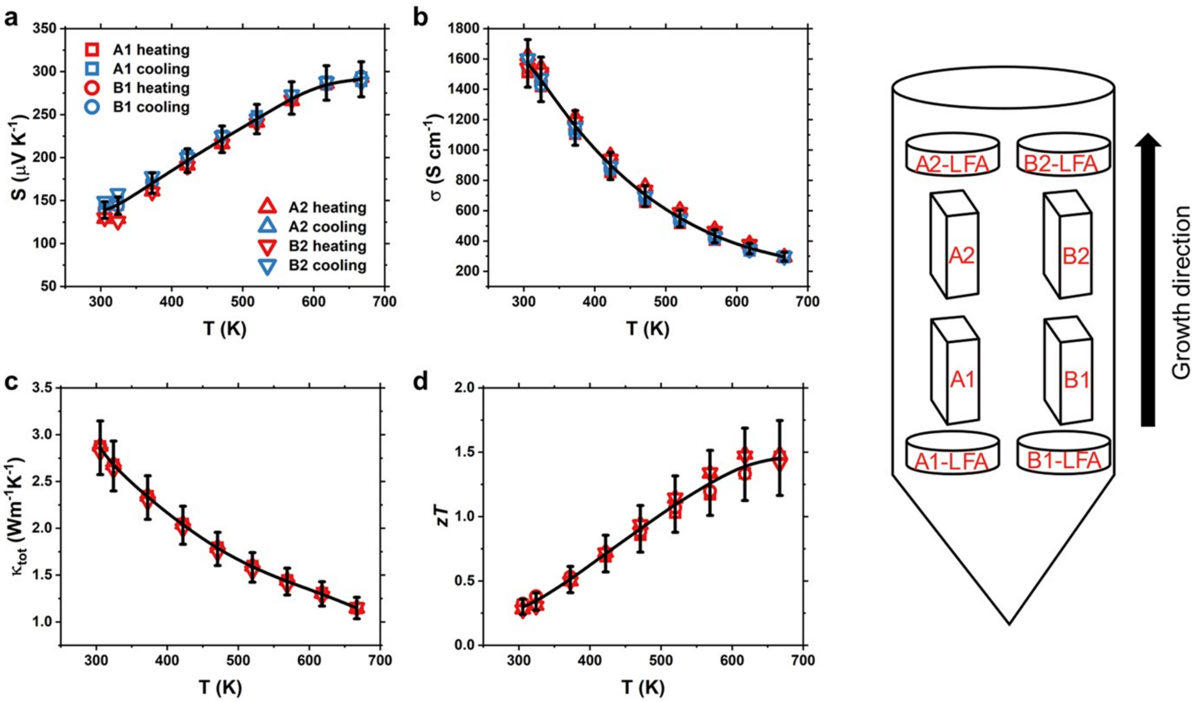

Supplementary Fig. 23| Comparable measurements with heating and cooling curves of 1% Fe_2As-doped Te using the ZEM-3 measurement system and LFA 457 (a) Seebeck coefficient (b) electrical conductivity (c) total thermal conductivity, and (d) dimensionless figure-of-merit (*zT*). All samples were carefully prepared with the same synthetic conditions.

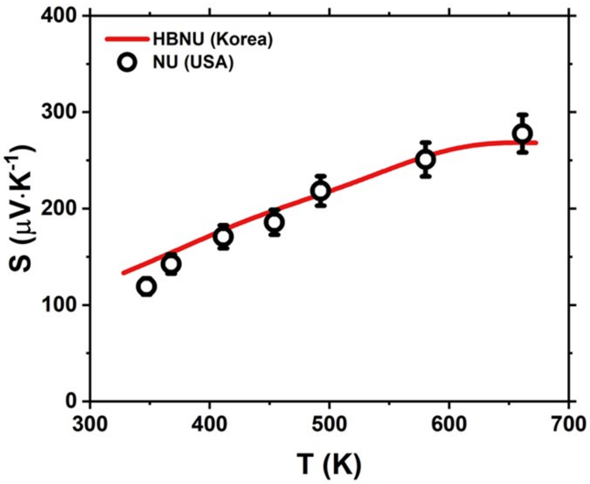

Supplementary Fig. 24| International thermoelectric property measurements for 1% Fe_2As-doped Te. Red lines denote the reported data measured in Hanbat National University (HBNU), while circles denote the data measured in Northwestern University (NU). The Seebeck coefficient was measured using a commercial apparatus in HBNU, while home-built apparatus was used in NU. The thermal conductivities were measured using a same apparatus (LFA 457, Netzsch).

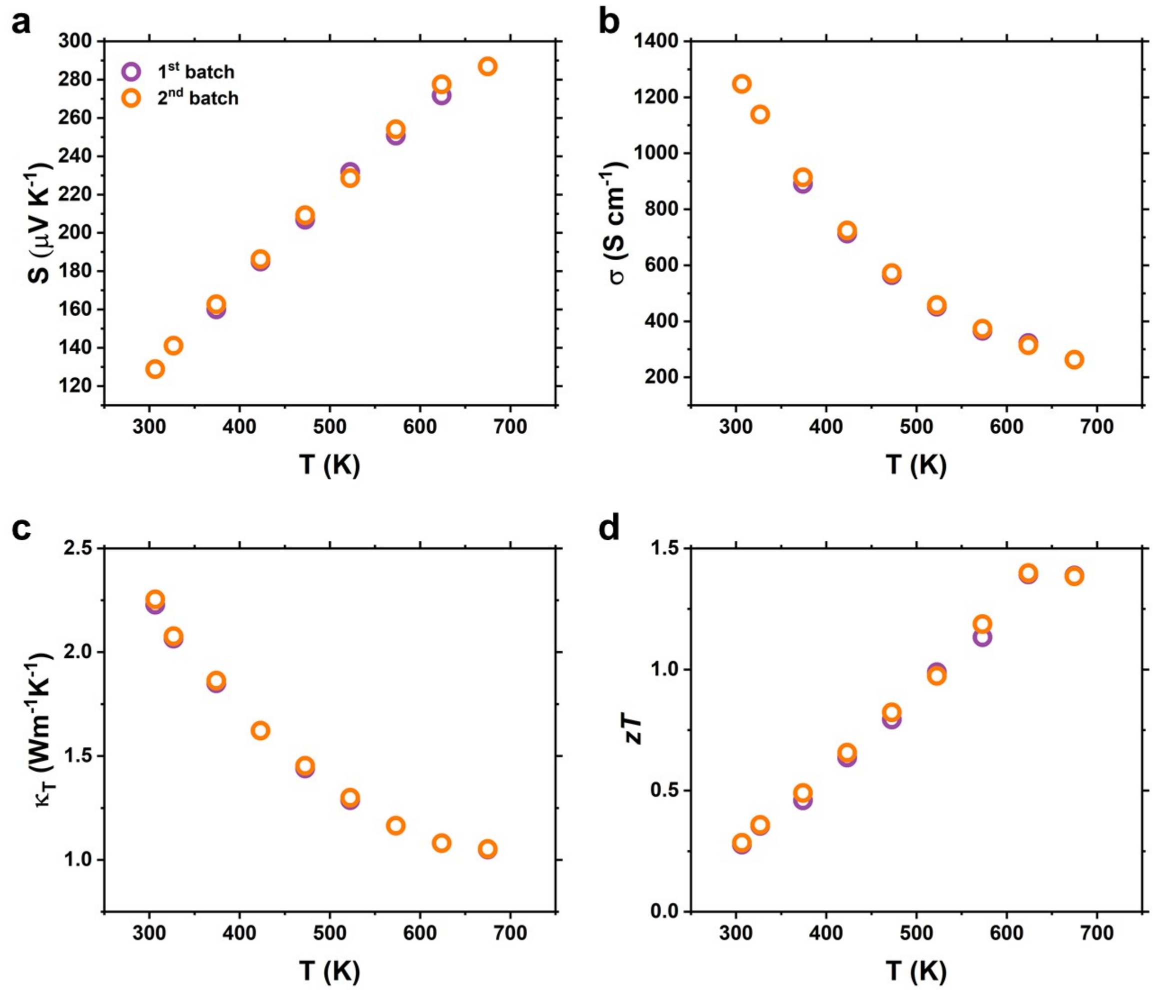

Supplementary Fig. 25| Reproducibility of 1% Fe_2As doped Te from two different batches (a) Seebeck coefficient, (b) electrical conductivity, (c) power factor, (d) total thermal conductivity, and (e) dimensionless figure of merit (*zT*). All samples were carefully prepared with the same synthetic conditions.

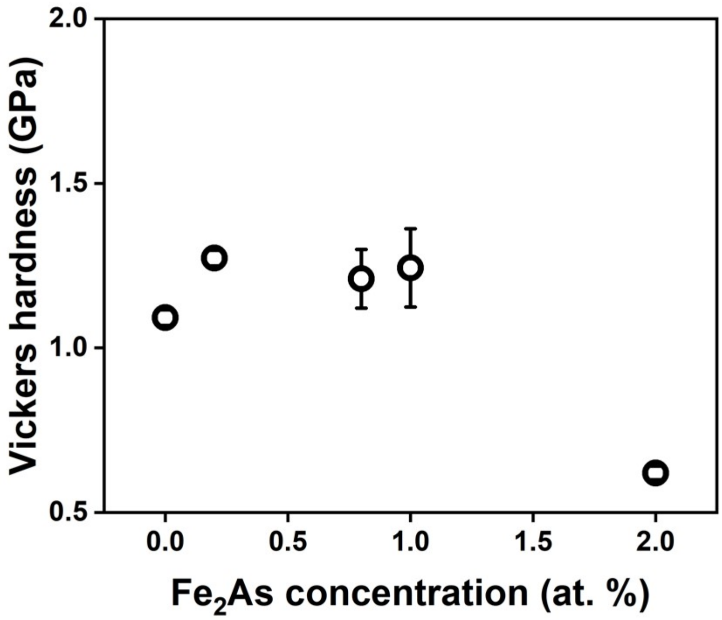

Supplementary Fig. 26| Vickers hardness values of pure and Fe_2As-doped Te samples measured by nanoindentation. The error bar denotes standard deviation of the measurement (n=8).

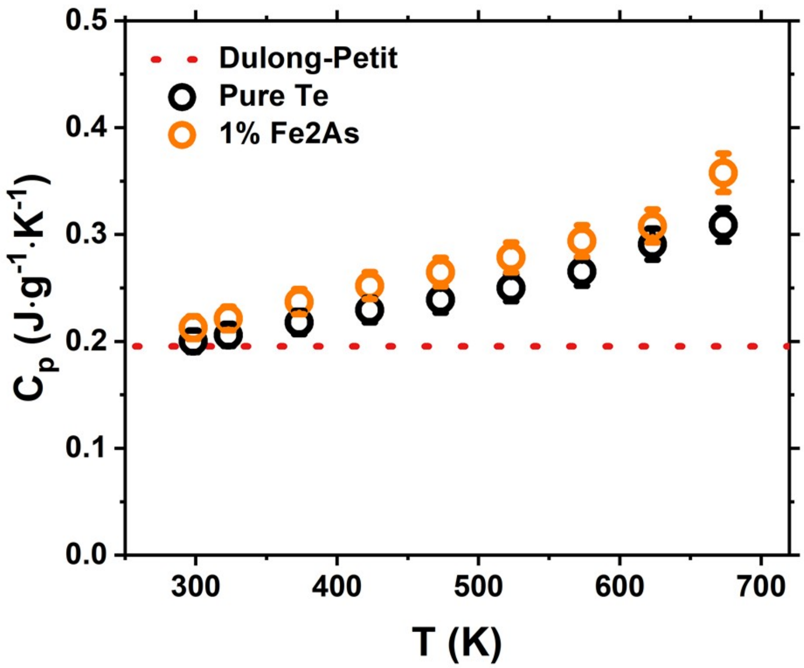

Supplementary Fig. 27| Specific heat capacity of pure Te and 1% Fe_2As-doped Te crystal measured by Netzsch Korea. Red line denotes the theoretical Dulong-Petit heat capacity limit of Te (0.195 $Jg^{-1}K^{-1}$).

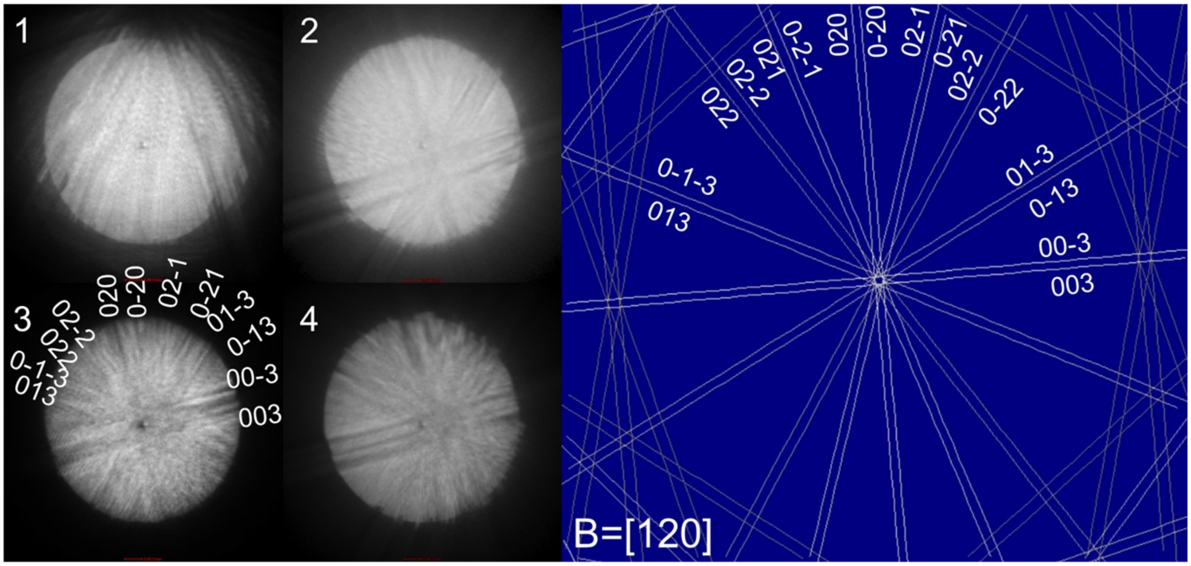

Supplementary Fig. 28| The Kikuchi pattern acquired at region 1 to 4 in the main text and the simulated Kikuchi pattern of Te viewed along the [120] zone axis.

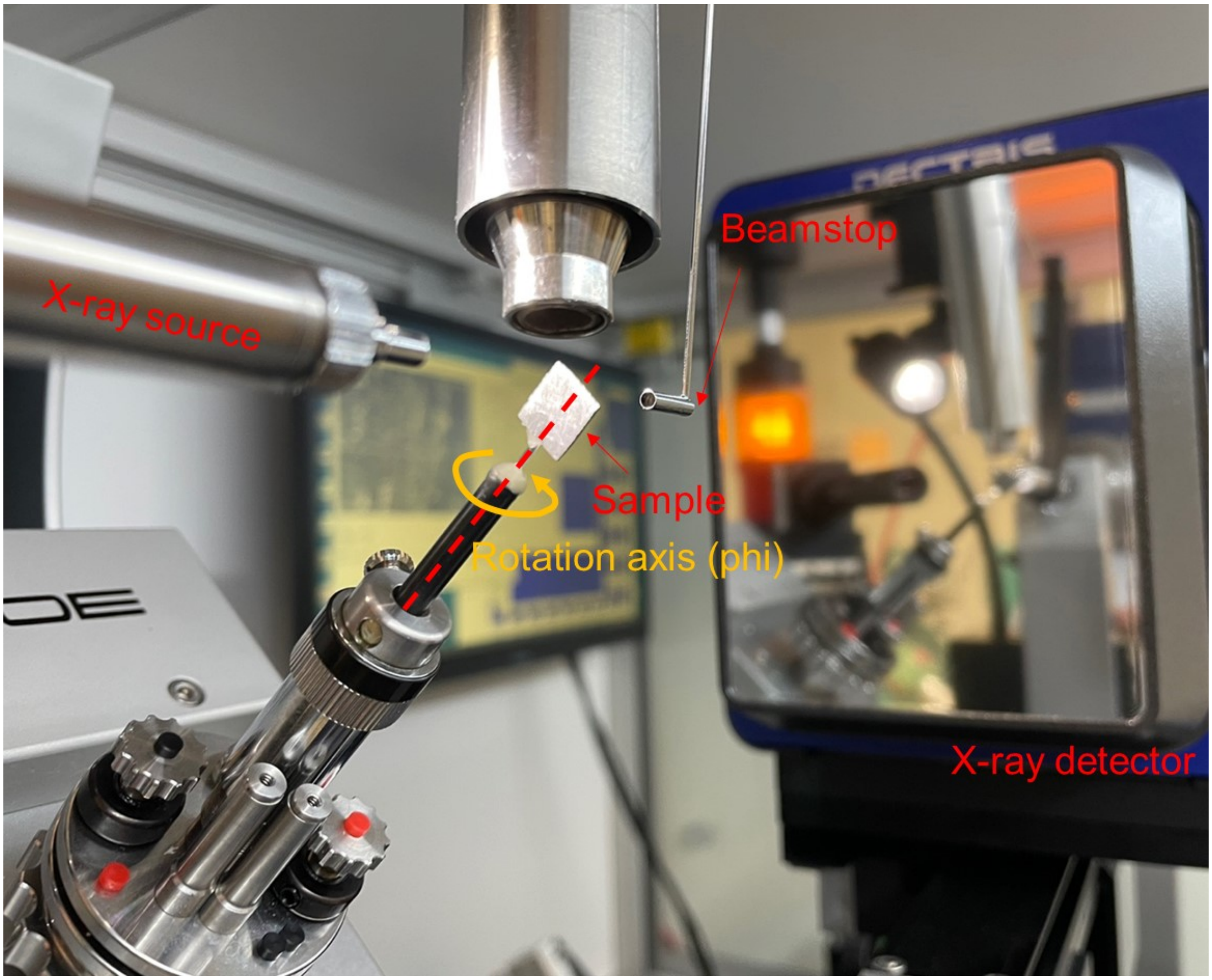

Supplementary Fig. 29| Configuration of the STOE STADIVARI X-ray diffractometer used to conduct an angle-dependent X-ray diffraction experiment.